Supporting Material

Section 2.3.3: Extra notes of factors in the flood risk baseline model

TWI measures the land surface's water accumulation capacity based on slope and elevation, effectively predicting areas prone to overland flow by quantifying the role of topography on the hydrological process of river flood [1]. Vegetation cover, indicated by NDVI, can influence local hydrodynamics by mitigating flood intensity and speed, thus reducing flood risk [2].

Hydrological factors usually use multi-level buffers based on distance from river systems to assess potential risks, in addition to direct characterization by distance alone [3, 4]. We set 4 levels of buffer zones based on the Euclidean distance to river systems, thereby divided the proximity level into 4 levels (Table S1).

For vulnerability factors, areas with high population-asset density are significantly more vulnerable to extreme rainfall and flood than areas with low population output, as the former experience greater absolute losses regardless of local disaster prevention conditions [5-7].

Table S1. Classification criteria of Proximity Level to river systems

Proximity level to river systems	Width of Buffer zone for main streams/km	Width of Buffer zone for tributaries/km	Width of Buffer zone for lakes/km
1	5	3	2
2	5 ~ 10	3 ~ 6	2 ~ 4
3	10 ~ 15	6 ~ 9	4 ~ 6
4	> 15	> 9	> 6

Section 2.3.4: Flood risk in future scenarios

Here are the specific steps to estimate RMAX3 in 2030s under RCP4.5 scenario based on NEX-GDDP dataset:

Step 1 Clip out the daily rainfall results of the wet season in the PLEZZ in 2020, calculate the RMAX3 of 2020 under one model, and then take the mean value of 21models as RMAX3 in 2020;

Step 2 Repeat Step 1 to obtain RMAX3 for 2018-2022, average them as RMAX3 for 2020s, and similarly obtain RMAX3 for 2030s;

Step 3 Calculate the change ratio of RMAX3 in 2030s, and multiple this ratio by the actual RMAX3 to obtain the estimation of RMAX3 for 2030s under RCP4.5 scenario. Same process for other periods.

Section 3.1.1: Analysis of historical precipitation and inundation scenarios

✧ **Results of rainfall amount (RA) and rainstorm frequency (RF)**

According to Figure S1, RA in 2017 is larger than that in 2020. The average of RA for all grids in 2017 is 1033.0 mm, greater than 1016.3 mm in 2020. In fact, the 2020 flood has the most intense rainfall in recent years. Therefore, RA cannot reflect the extreme of the flood well as accurately as maximum 3-day rainfall (RMAX3). For RF, it is worse. In Figure S2, the number of rainstorm days per year has no obvious difference. The severity of the hazard in 2020 is not manifested, even less severe than that in 2016 and 2017. The correlation coefficient between the multi-year average of these two factors and that of RMAX3 is 0.85 and 0.86 respectively,

presenting a high linear correlation.

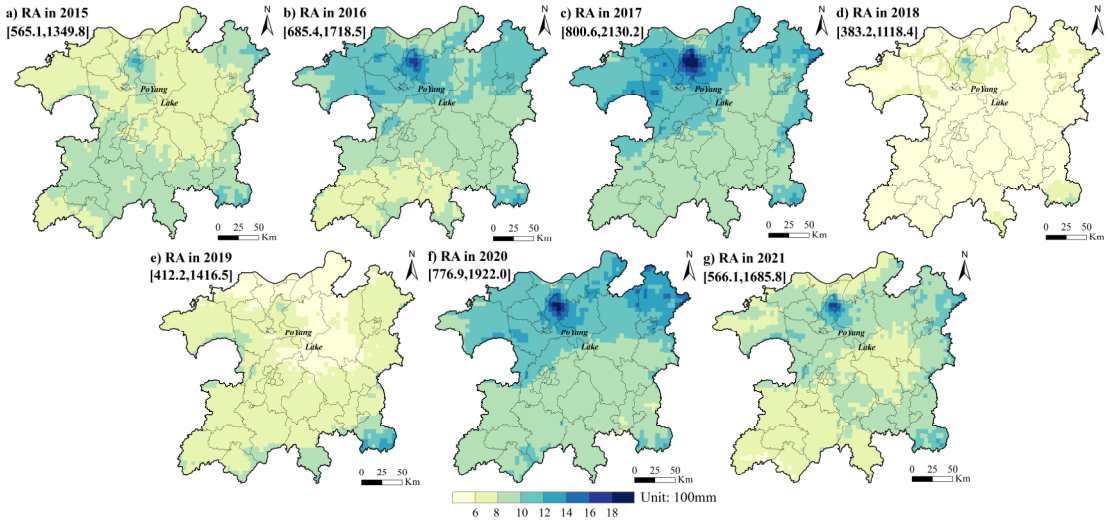

Figure S1. Spatial distribution of RA in the wet season over the years 2015-2021.

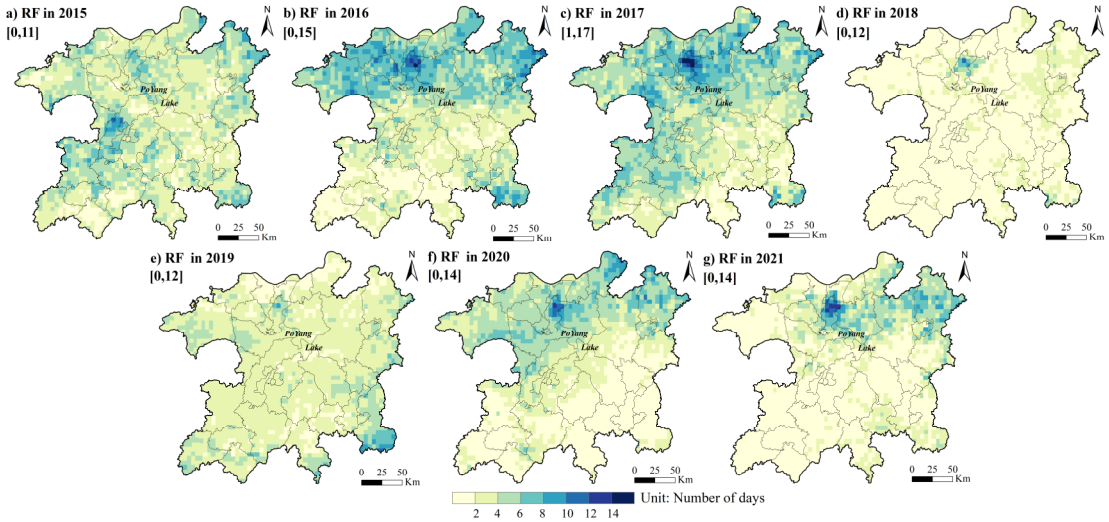

Figure S2. Spatial distribution of RF in the wet season over the years 2015-2021. Rainstorm is defined as daily rainfall greater than 50 mm.

✧ Numerical distribution comparison of RMAX3 in 2020, 2016 and 2017

RMAX3 of 2020 has an overwhelming proportion in the high-value interval (above 230 mm), and the average value is much higher. About 9,254 km^2 area was subject to persistent rainstorm (exceeding 150 mm) in 2020 more than in 2017 and 12,680 km^2 more than in 2016. Therefore, the strong concentrated precipitation in Poyang Lake Eco-economic Zone (PLEEZ) in 2020 is the most intense event in the past seven years.

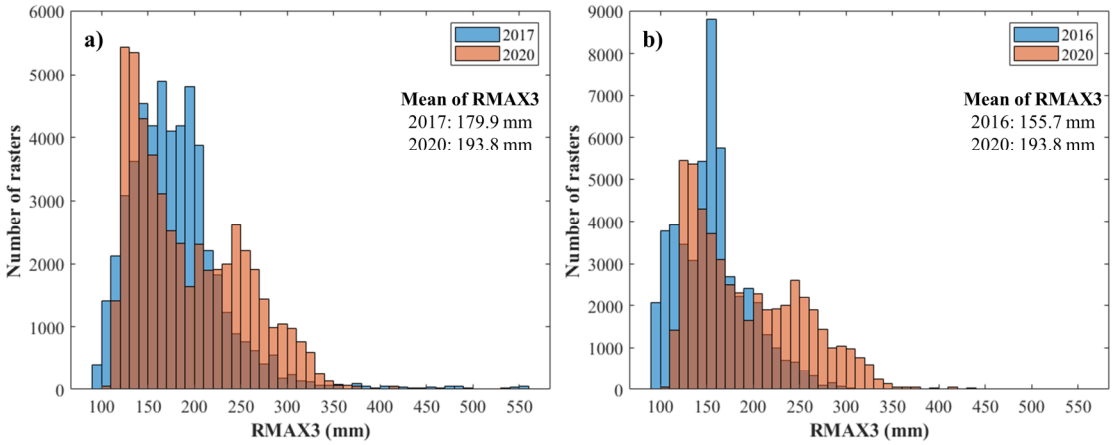

Figure S3. Statistical results of RMAX3 for all grids in PLEEZ in the year with major flood. (a) Histogram of RMAX in 2017 and 2020. **(b)** Histogram of RMAX in 2016 and 2020.

✧ Annual flood evolution and the maximum range of inundation during 2015-2021

The number of SAR images available for the wet season in seven years from 2015 to 2021 is shown in Table S2. Combined with Figure S4, the annual flood evolution process can be reviewed.

Table S2. Statistics on the flood evolution process over the years 2015-2021

Year	No. of A-satellite images	No. of B-satellite images	Four stages of flood evolution process (Date: Month/Day)				Maximum inundation area (km^2)
2015	8	-	6/15 ~ 6/17	6/17 ~ 7/11	7/11 ~ 7/23		1048
2016	6	-	6/11 ~ 7/5	7/5 ~ 8/10			978
2017	7	7	6/12 ~ 6/24	6/24 ~ 7/6	7/6 ~ 7/18	7/18 ~ 7/30	1583
2018	6	6	7/1 ~ 7/13	7/13 ~ 7/25			864
2019	8	8	6/2 ~ 6/14	6/14 ~ 7/8	7/8 ~ 7/20	7/20 ~ 8/1	1070
2020	8	8	6/20 ~ 7/2	7/2 ~ 7/14	7/14 ~ 7/26	7/26 ~ 8/7	2001
2021	8	8	6/27 ~ 7/9	7/9 ~ 7/21			940

***Note:** The flood evolution stages represented by different colors are consistent with those in the legends of Figure 5&S4.

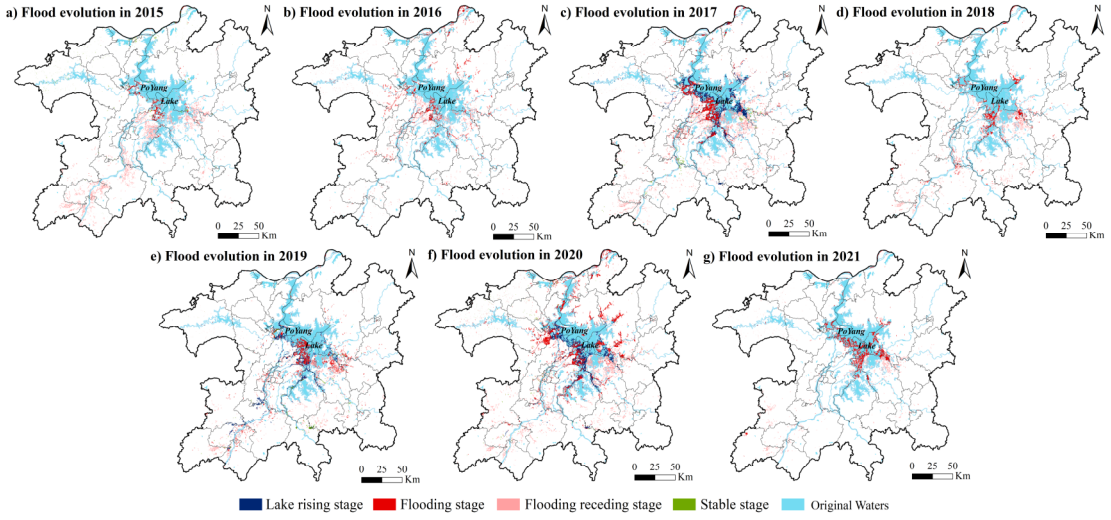

Figure S4. Spatial distribution of the flood evolution process over the years 2015-2021

After the flood process analyses, the maximum inundation area was resampled to 1 km to obtain the spatial distribution of historical inundation scenarios (Figure S5).

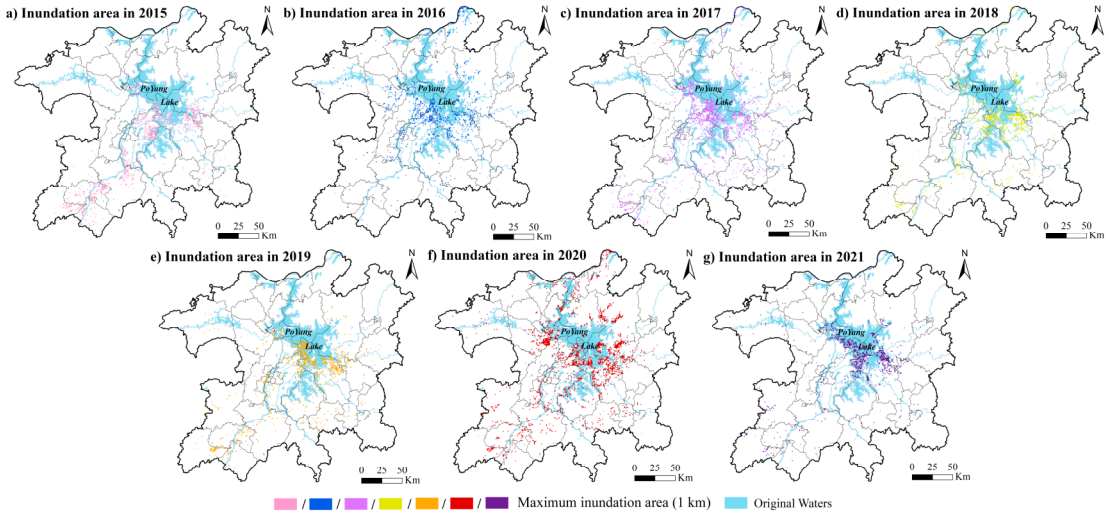

Figure S5. Spatial distribution of historical inundation scenarios over the years 2015-2021

Section 3.1.2: Extra explanation for factors

The Pearson and Spearman's Correlation are usually used to verify the collinearity between each two factors. The former is only applicable to continuous variables, while the latter is more sensitive to outliers. All values in both correlation coefficient matrixes were less than 0.7, indicating that there was no significant linear relationship (Figure S6). The variance inflation factor (VIF) concerns the multicollinearity between one variable and other variables. A serious multicollinearity problem exists in the case of the TOL less than 0.1 and VIF (the reciprocal of TOL) greater than 10. Obviously, there was also no multicollinearity problem among the factors based on Table S3.

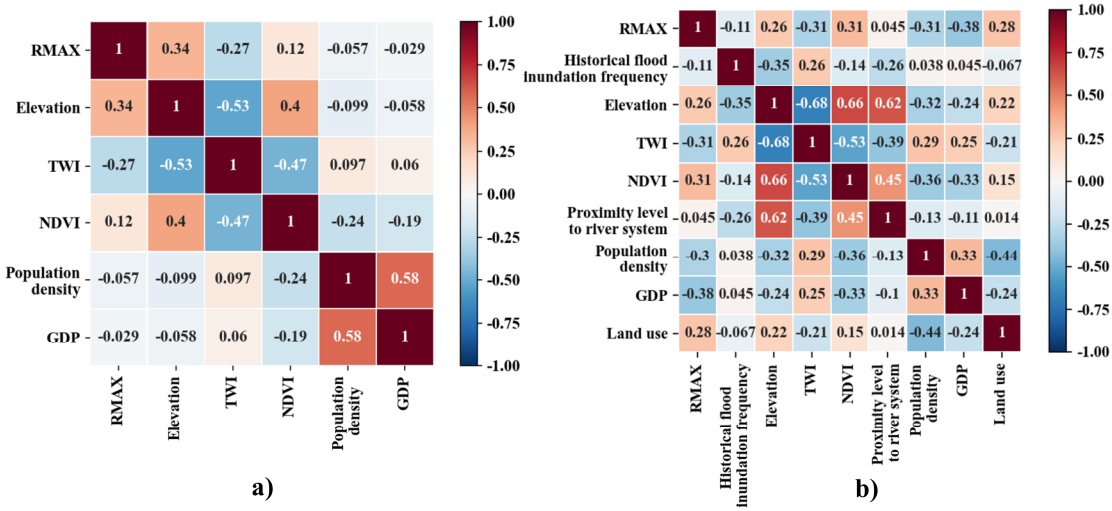

Figure S6. Collinearity analysis results between each two variables. (a) Pearson correlation coefficient matrix. **(b)** Spearman's correlation coefficient matrix.

Table S3. Multicollinearity results of factors

Factor	TOL	VIF
RMAX	0.560	1.785
Elevation	0.220	4.546

TWI	0.202	4.959
NDVI	0.276	3.625
Population density	0.226	4.422
GDP	0.243	4.112

Section 3.2.1: Spatial distribution of future trends of assessment factors

The following three figures show the spatial change of RMAX3, population density, and GDP in different periods under different future scenarios, respectively.

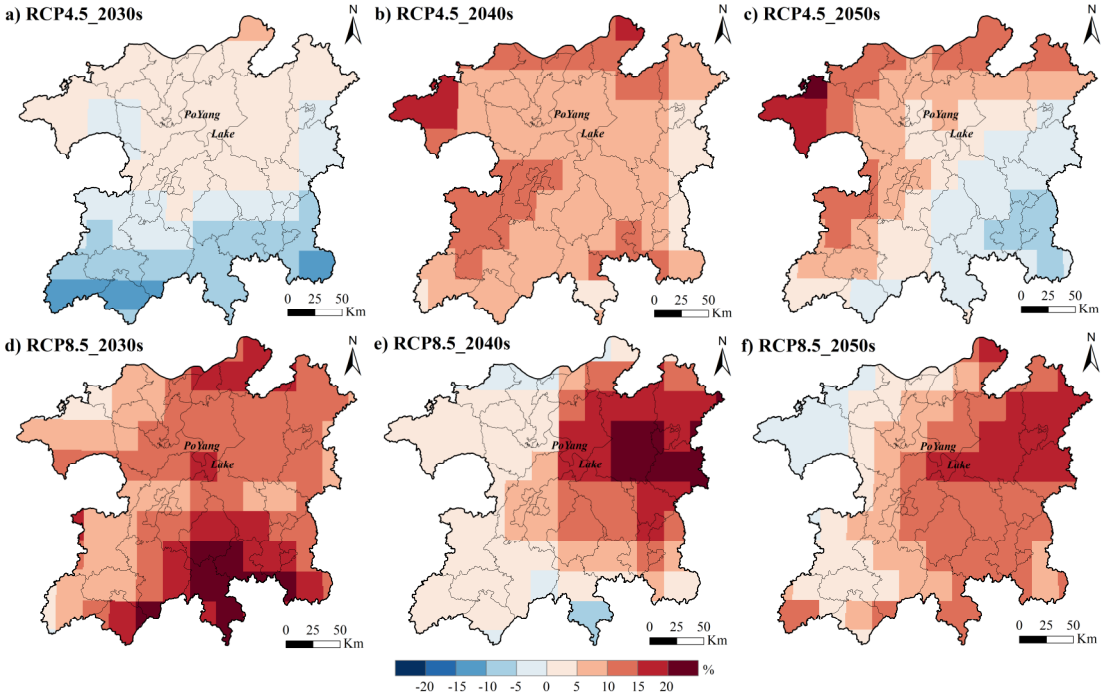

Figure S7. Spatial change ratio of RMAX3 in different future periods (compared to 2020s).

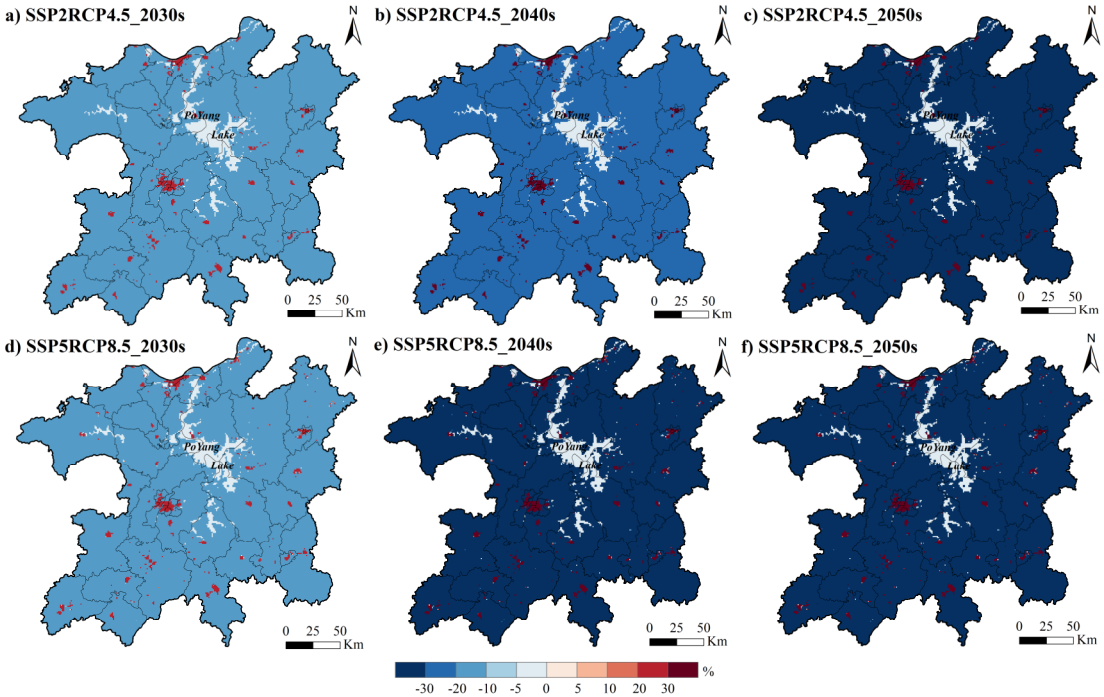

Figure S8. Spatial change ratio of population density in different future periods (compared to 2020s).

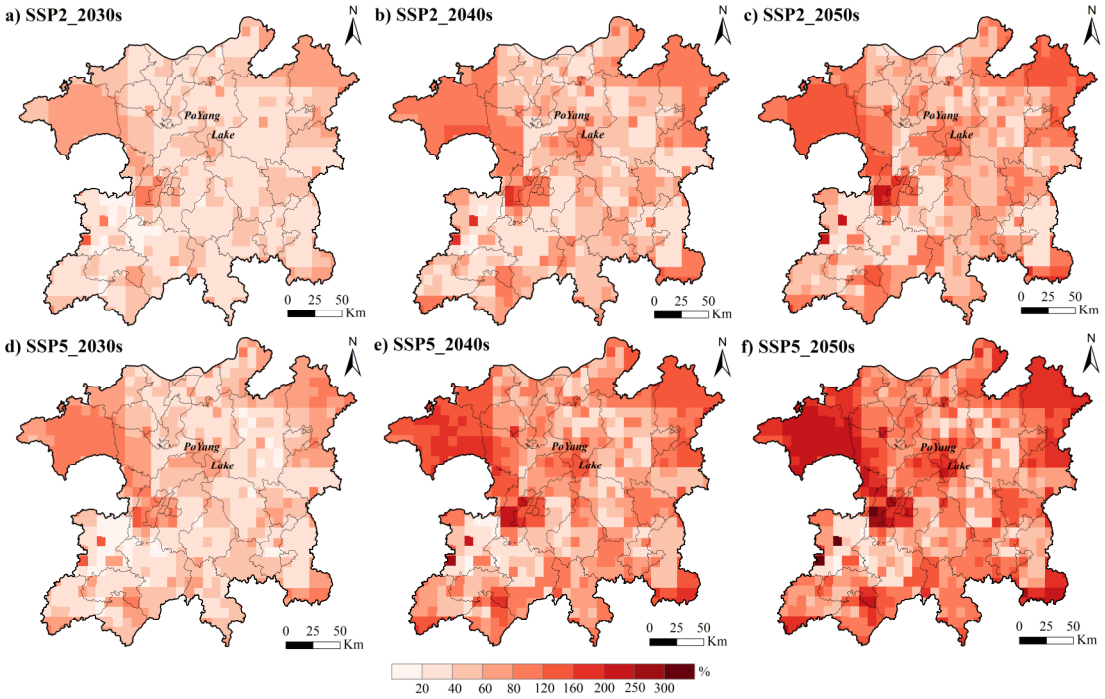

Figure S9. Spatial change ratio of GDP in different future periods (compared to 2020s).

The natural drivers affecting land use inputted in the FLUS model include elevation, slope, aspect, clay content, soil type, and topographic wetness index, and socio-economic drivers includes GDP, population density, the distance to highways, national highways, urban arterials, railroads, buildings, city centers, town centers, point of interest, and transportation nodes. Table S4 statistics the number of grids projected by the model and the expected number of grids for each land use type. High accuracies prove that the FLUS model achieves reasonable results.

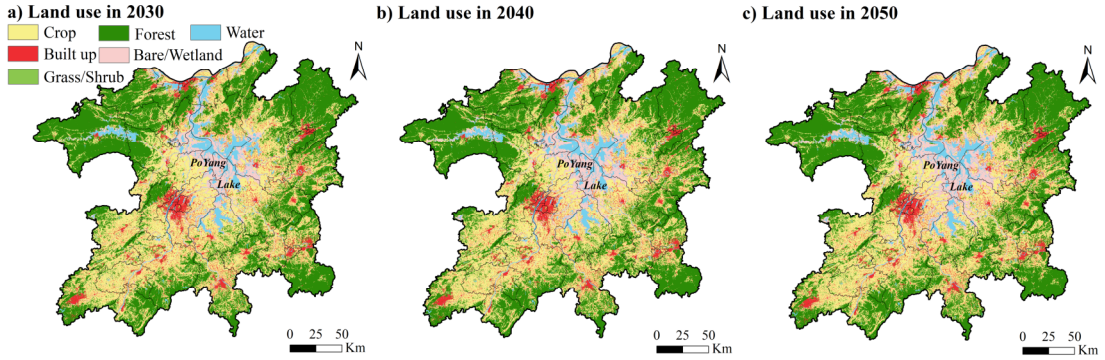

Figure S10. Spatial distribution of land use in different future periods predicted by FLUS model.

Table S4. Model prediction accuracy of land use

Number of grids	**2030**			**2040**			**2050**		
	Theory	Projection	**Accuracy**	Theory	Projection	**Accuracy**	Theory	Projection	**Accuracy**
Crop	1903750	1903745	**0.99**	1853994	1853992	**0.99**	1805768	1805765	**0.99**
Built up	396389	396390	**0.99**	400461	400465	**0.99**	404381	404383	**0.99**
Grass/Shrub	20397	20643	**0.99**	8705	8705	**1**	4664	4664	**1**
Forest	2133710	2133710	**1**	2105857	2129376	**0.99**	2078361	2127296	**0.98**
Water	295169	295169	**1**	314927	291407	**0.93**	339604	290670	**0.86**
Wetland/Bare	367085	366843	**0.99**	432555	432555	**1**	483722	483722	**1**

***Note:** "Theory" represents the expected number of grids calculated according to the Markov chain, and "Projection" represents the number of grids simulated by the model.

Section 4.1: Extra explanation for flood inundation-prone zone

The process of generating the flood inundation-prone is as follows. First, take the historical flood inundation frequency (Figure S11a, the same as Figure 6b) as the input of Optimized Hot Spot Analysis tool in ArcGIS, then can get the hot spots of flood inundations (that is red and orange clusters identified in Figure S11b). The hot spots all pass the significance test with more than 90% confidence, and no cold spots. Convert these hot spots into polygon, thereby get the flood inundation-prone zone (Figure S11c).

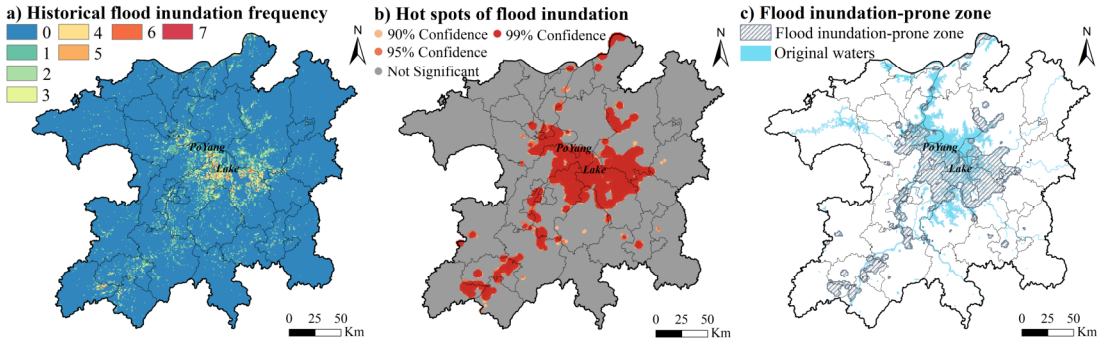

Figure S11. Process of generating the flood inundation-prone zone.

The proportion of annual inundation areas falling within the flood inundation-prone zone for past events between 2015 and 2021 is 74%, 68%, 72%, 79%, 75%, 62% and 80%, respectively, with an average of 73%, indicating that this zone's good inclusion of historical inundation. Apart from this, this zone has a favorable ability to perceive the high risk based on the fact that in the baseline scenario (Figure 7a), it can encompass 82.9% of the very high risk and 35.6% of the high risk level area with covering 11.4% of the PLEEZ itself, while meantime only encompass 0.3% and 6.3% of the very low risk and low risk level areas, respectively.

Section 4.2: Reliability of future evaluation factors

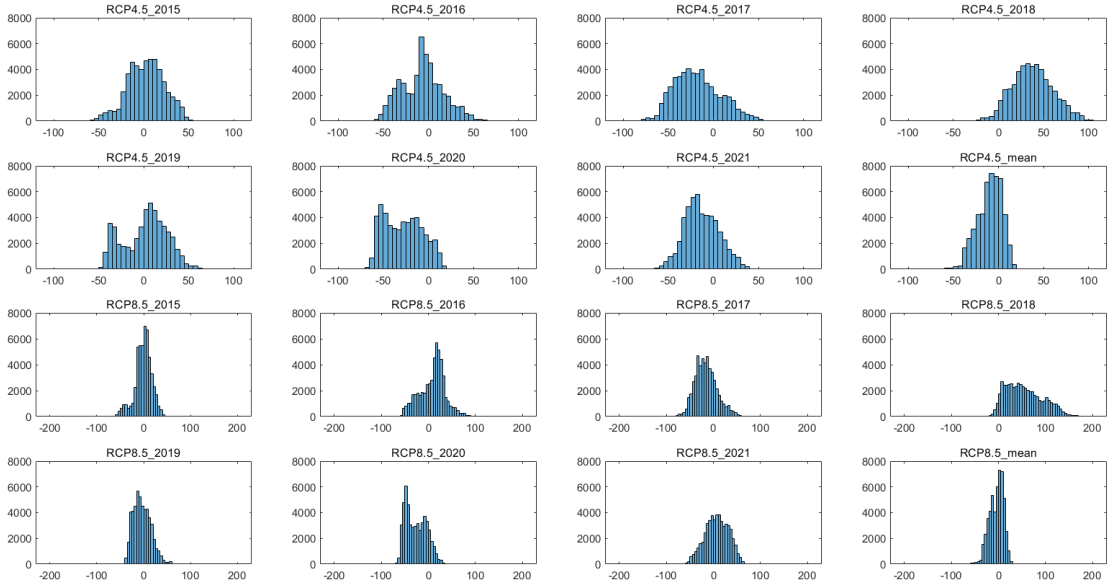

Figure S12. Error Histogram of RMAX3 between the future projected precipitation dataset (NEX-GDDP) and the historical satellite-precipitation dataset (CHIRPS). The horizontal axis represents the error and the

vertical axis represents the frequency of the error.

For population, although the range of the difference between the projected results and the actual one in 2020 is relatively large on all grids (Figure S13e), 50% of the errors lie within the interval [-103, -8] and 87% of the errors after removing outliers lie within the interval [-246, -133] (Figure S13d). The mean values of the errors are 30 and 14, respectively, and the median is -38. These indicate that the overall errors are still within a reasonable range. Meanwhile, the spatial distribution pattern in 2020 reflected by the future population data is close to the actual one as the spatial correlations reach more than 0.85 (Figure S13a&b&c), proving that this dataset can effectively simulate the population situation.

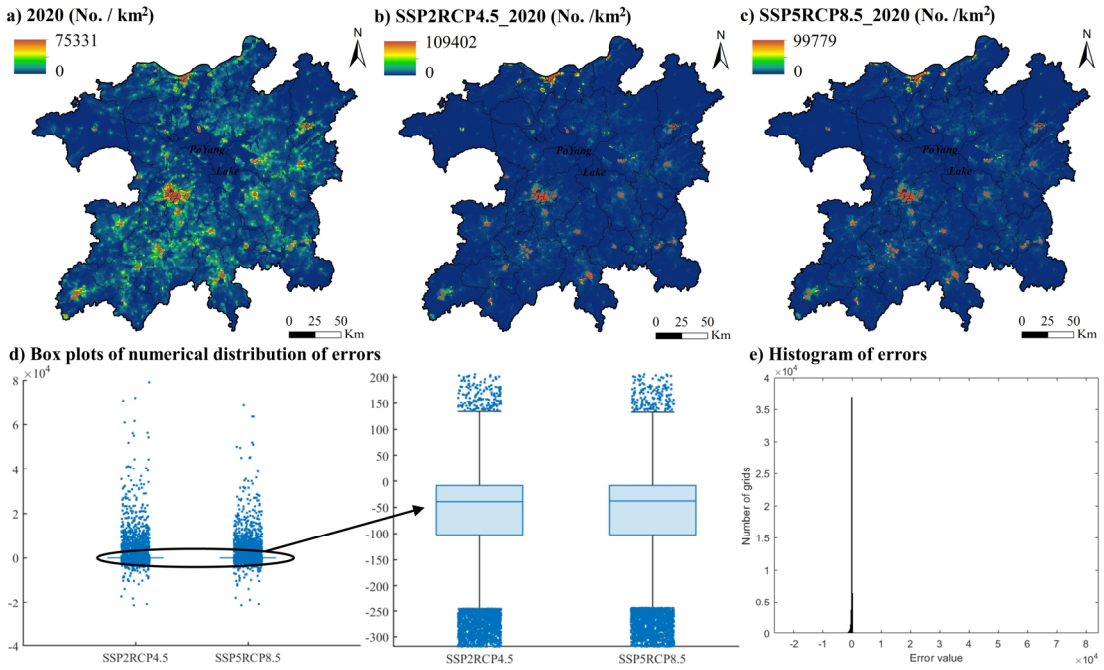

Figure S13. Error Analysis of population density between the future projected dataset and the historical dataset in 2020. (a)&(b)&(c) are the spatial distributions of the actual and projected population density in 2020. **(d)** Box plots of the difference between predicted and actual population density for all grids, the arrow pointing to the box part after zooming in. **(e)** Histogram of all error values under the SSP2RCP4.5 scenario (similar distribution for the SSP5RCP8.5 scenario).

For GDP, first, the future predicted results in 2020 coincide with the actual spatial distribution pattern and have spatial correlations of up to 0.6 (Figure S14a&b&c). Except for partial grids error percentages that are too high (Figure S14e), 50% of error percentages are within the interval [-84%, -45%] and 89% of them after removing outliers are within the interval [-99%, -17%] (Figure S14d). The mean and median values are -49% and -74%, respectively. Apparently, the predict of future GDP is smaller than the actual, but the difference is no more than 100%. Despite that the prediction accuracy is not as high as the population, we consider this to be acceptable as the best choice among the available relevant datasets given its 10 km resolution (10 times that of the population data).

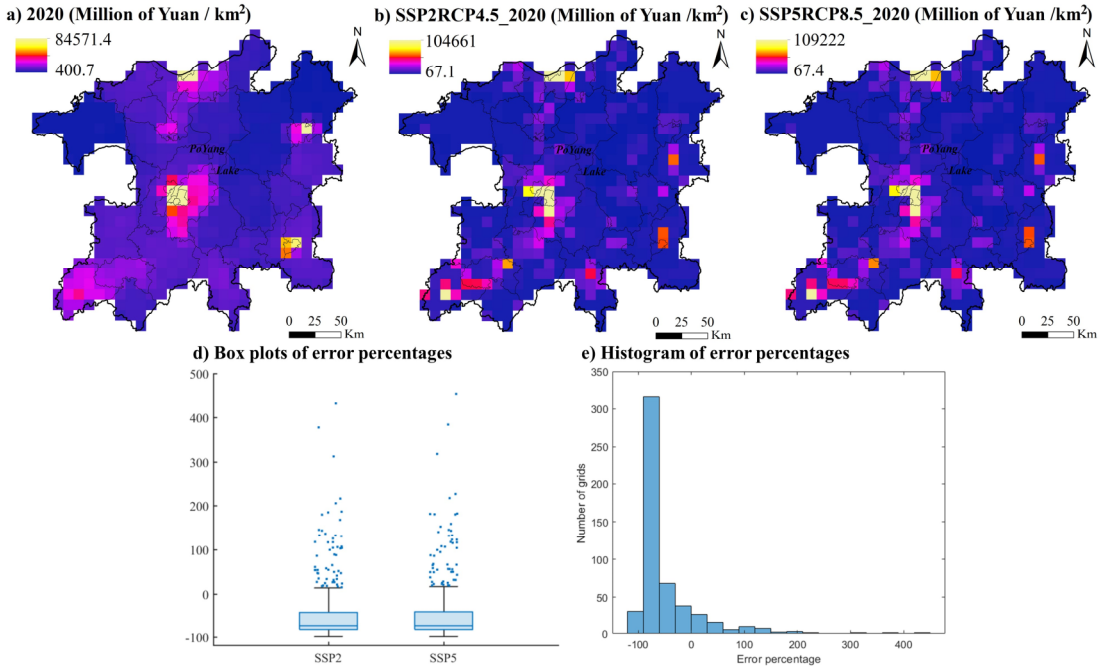

Figure S14. Error Analysis of GDP between the future projected dataset and the historical dataset in 2020. **(a)&(b)&(c)** are the spatial distributions of the actual and projected GDP in 2020. **(d)** Box plots of the error percentages of projected GDP over actual for all grids. **(e)** Histogram of all error percentage values under the SSP2RCP4.5 scenario (similar distribution for the SSP5RCP8.5 scenario).

Section 4.3: Further application in other catchments for applicability

We apply the framework to the Huaihe River Basin (Figure S15), another flood-ravaged area in southern China for years located in the north of the PLEEZ, which is also one of the most affected areas during the catastrophic summer flood in 2020.

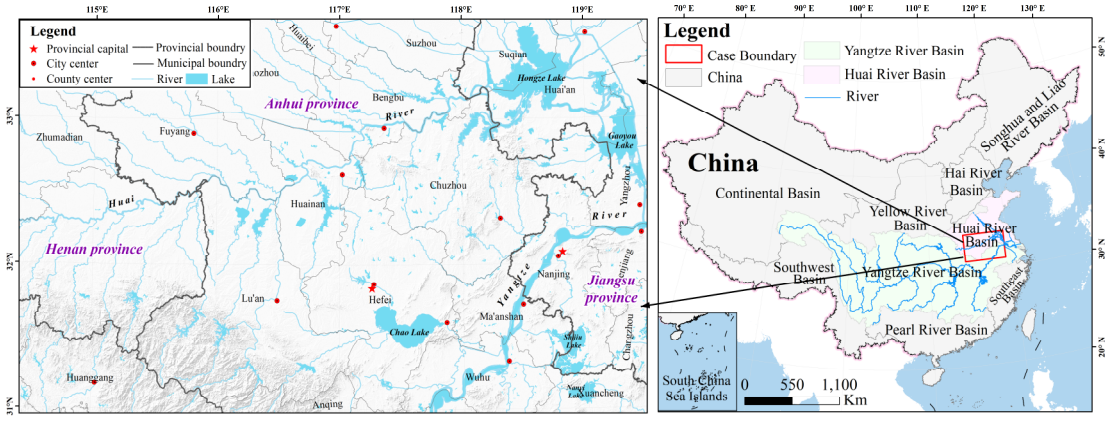

Figure S15. Overview of the case study area of the Huai River Basin (including partial Yangtze River Basin).

Two sets of experiments are set up here. First, Experiment A constructs the framework based on historical floods and rainfall from 2010 to 2019, and then uses it to test the capacity to cope with extreme floods (represented by 2020) and regular floods (represented by 2021). The basin-wide floods that occurred in 2003 and 2007 were the most destructive disaster events in the historical record for the past 20 years in this region. Experiment B adds the extreme inundation and precipitation scenarios from these two years to Experiment A, thereby updating the framework. Another remote sensing data adopted here to extract inundation is derived from MODIS products

on GEE, provided by NASA LP DAAC[1], considering no Sentinel-1 data before 2014. Figure S16 shows the spatial distribution of each zone derived from the framework in these two experiments and the extent of inundation in 2020 and 2021. Table S5 provides statistics on the percentage of inundation area covered by different response ranks in these two years.

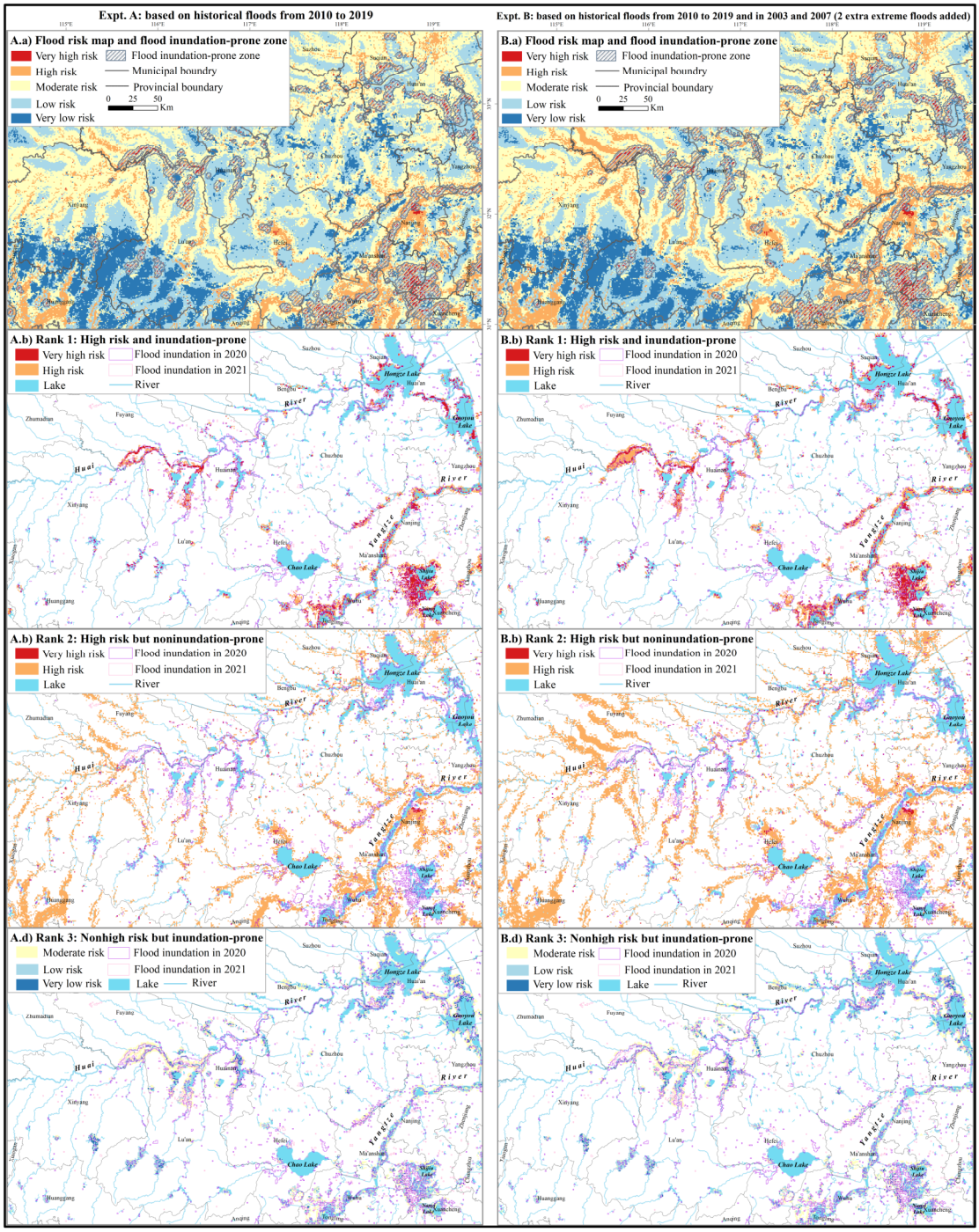

Figure S16. A controlled experiment of the framework applied in the Huaihe River Basin. For Expt. A on the left column, the range of historical flood events for framework construction is from 2010 to 2019. For Expt. B on the right column, two extra extreme floods in 2003 and 2004 is added into the framework construction. Subfigure A.a presents the flood risk map and inundation-prone zone, and subfigures A.b, c, d present 3 response rank respectively. The same for Subfigure B.a &b &c &d.

[1] The MODIS data and products including MOD09GQ.061 and MYD09GQ.091 are from the GEE platform, provided by NASA LP DAAC at the USGS EROS Center (https://developers.google.com/earth-engine/datasets/catalog/MODIS_061_MOD09GQ; https://developers.google.com/earth-engine/datasets/catalog/MODIS_061_MYD09GQ).

Table S5. The validation of response performance of the framework to extreme and regular floods in Huaihe River Basin

Experiment type	Management perspective	The inundation scenario in 2020 (4099 km^2)			The inundation scenario in 2021 (2934 km^2)		
		Coverage area (km^2)	Coverage ratio*	Total ratio	Coverage area (km^2)	Coverage ratio*	Total ratio
Expt. A: based on historical floods from 2010 to 2019	Rank 1	2044	49.87%		1764	60.12%	
	Rank 2	723	17.64%	78.82%	561	19.12%	85.68%
	Rank 3	464	11.32%		189	6.44%	
	Flood high-risk zone	2767	67.5%	-	2325	79.24%	-
	Flood inundation-prone zone	2508	61.19%	-	1953	66.56%	-
Expt. B: based on historical floods from 2010 to 2019 and in 2003 and 2007 (2 extra extreme floods added)	Rank 1	2397	58.48%		1837	62.61%	
	Rank 2	761	18.57%	85.51%	559	19.05%	87.83%
	Rank 3	347	8.47%		181	6.17%	
	Flood high-risk zone	3158	77.04%	-	2396	81.66%	-
	Flood inundation-prone zone	2744	66.94%	-	2018	68.78%	-

***Notes:** The coverage ratio is the proportion of inundation area covered by a certain management perspective to the total actual inundation area. For example, 49.87% means that in the framework constructed based on the years 2010 to 2019, Rank 1 covers 49.87% of the actual inundated area in 2020.

In Experiment. A, the multiperspective provided by the framework (i.e., Ranks 1, 2 and 3 in Table S5) identifies a total of 78.82% of the 2020 inundation, an improvement of 11.32% over relying only on the flood high-risk perspective (identified 67.5%). This gain comes from Rank 3, characterized by non-high risk but inundation-prone. This means that if our framework were to be applied to the local management, the 464 km^2 would have the opportunity to implement more rigorous monitoring and forecasting to mitigate losses. Moreover, unlike the single high risk perspective, the framework also plans the 67.5% in two parts: 49.87% in Rank 1 and 17.64% in Rank 2. This makes it easier for the authorities to optimize the allocation of disaster reduction resources. For example, residents within 723 km^2 in Rank 2 would have a chance to be warned in time (which was previously overlooked because these areas were less prone to flooding) and relocated to a safe place. Simultaneously, more human and financial resources can be devoted to strengthening disaster prevention in the 2044 km^2 area in Rank 1.

After adding the historical extreme scenarios of 2003 and 2004 in Experiment. B, the updated framework's multipespective significantly improves the identification rate of the 2020 inundation by 6.69%. This improvement comes mainly from Rank 1, which itself increases by 8.61% from 49.87% to 58.48%. It is a particularly desirable outcome for decision makers, because more priority governance invested in Rank 1 will not be wasted, just as more of the 2020 inundation areas occur within Rank 1, as illustrated in Subfigure S16.A.b and B.b. As reflected by less area in Subfigure S16.B.d compared to A.d, another improvement is the decrease in the identification rate of Rank 3 from 11.32% to 8.47%, which indicates that unforeseen disasters that originally occurred outside the high-risk zone are reduced after updating the framework. In other words, by incorporating more extreme historical scenarios, our framework can further raise the efficiency of resource utilization and weaken the management uncertainty.

For regular flood events such as 2021, the framework is able to handle upcoming floods with more confidence compared to extreme years. 85.68% of the inundation occurs within the multiperspective zones, a 6.86% improvement over the 2020 extreme scenario. The inclusion of

additional extreme historical scenarios also further optimizes the risk management of periodic floods, as evidenced by the overall identification rate increasing to 87.83%.

In summary, the Huaihe River Basin case demonstrates that the framework reduces the decision-making uncertainty of floods, especially for extreme events, and has practical applications for other flood-prone basin or catchments.

References

1. Manfreda, S., M. Di Leo and A. Sole. "Detection of flood-prone areas using digital elevation models." *Journal of Hydrologic Engineering* 16 (2011): 781-90.
2. Parsian, S., M. Amani, A. Moghimi, A. Ghorbanian and S. Mahdavi. "Flood hazard mapping using fuzzy logic, analytical hierarchy process, and multi-source geospatial datasets." *Remote Sensing* 13 (2021): 10.3390/rs13234761.
3. Hazarika, N., D. Barman, A. K. Das, A. K. Sarma and S. B. Borah. "Assessing and mapping flood hazard, vulnerability and risk in the upper brahmaputra river valley using stakeholders' knowledge and multicriteria evaluation (mce)." *Journal of Flood Risk Management* 11 (2018): S700-S16. 10.1111/jfr3.12237.
4. Wang, Y., Z. Li, Z. Tang and G. Zeng. "A gis-based spatial multi-criteria approach for flood risk assessment in the dongting lake region, hunan, central china." *Water Resources Management* 25 (2011): 3465-84. 10.1007/s11269-011-9866-2.
5. Duan, G., W. Zhao, Z. Hu and D. Fang. "An improved model of regional flood disaster risk assessment based on remote sensing data." Presented at 2011 19th International Conference on Geoinformatics, 2011. IEEE, 1-6.
6. Hu, P., Q. Zhang, P. Shi, B. Chen and J. Fang. "Flood-induced mortality across the globe: Spatiotemporal pattern and influencing factors." *Sci Total Environ* 643 (2018): 171-82. 10.1016/j.scitotenv.2018.06.197. https://www.ncbi.nlm.nih.gov/pubmed/29936160.
7. Liu, Y., S. Wang, X. Wang, D. Jiang, N. Ravindranath, A. Rahman, N. Htwe and T. Vijitpan. "Flood risk assessment in bangladesh, india and myanmar based on the ahp weight method and entropy weight method." *Geogr. Res* 39 (2020): 1892-906.